RSC Advances

PAPER

View Article Online
View Journal | View Issue

Open Access Article. Published on 14 August 2017. Downloaded on 2/18/2026 4:08:23 AM.
This article is licensed under a Creative Commons Attribution-NonCommercial 3.0 Unported Licence.

Check for updates

Cite this: *RSC Adv.*, 2017, **7**, 39594

Adsorptive removal of aqueous bezafibrate by magnetic ferrite modified carbon nanotubes†

Donghai Wu,[a] Jingjing Yao,[ab] Guanghua Lu,*[ab] Fuli Liu,[a] Chao Zhou,[a] Pei Zhang[c] and Matthew Nkoom[a]

Received 30th June 2017
Accepted 6th August 2017

DOI: 10.1039/c7ra07260k

rsc.li/rsc-advances

In this work, magnetic ferrite modified carbon nanotubes (MFe_2O_4/CNTs, M: Mn or Co) were synthesized and employed as adsorbents to remove emerging pollutant bezafibrate (BZF) from aqueous solution. The structural and surface properties of the prepared adsorbents were characterized, and the performances of the MFe_2O_4/CNTs were systematically investigated from adsorption kinetics and mechanistic points of view. Results showed that the fabricated MFe_2O_4/CNTs could integrate the advantages of CNTs and ferrite, thereby exhibiting an excellent adsorption performance and recyclability. The $MnFe_2O_4$/CNTs were more effective than $CoFe_2O_4$/CNTs for BZF adsorption. When the initial concentration of BZF was varied from 5 to 40 mg L^{-1}, the maximum adsorption capacity of $MnFe_2O_4$/CNTs and $CoFe_2O_4$/CNTs increased from 14.8 to 33.4 mg g^{-1} and 8.1 to 27.8 mg g^{-1}, respectively. Moreover, the Langmuir isotherm model and pseudo-second-order equation could elaborate well the adsorption of BZF on MFe_2O_4/CNTs. The thermodynamic analysis further revealed that the adsorptions were spontaneous processes. Based on measurements of surface and pore diffusion and the results of adsorption reactions, possible mechanisms were proposed to explain the adsorption process. This research indicates that the MFe_2O_4/CNTs are potentially applicable for the removal of BZF from aqueous solution.

1. Introduction

Pharmaceuticals and Personal Care Products (PPCPs) are widely used in medicine, industry, animal husbandry, agriculture, aquaculture and other fields.[1] PPCPs in the aqueous environment can affect natural ecosystems and aquatic organisms, even at low concentrations.[2] Bezafibrate (BZF) is a typical fibrate pharmaceutical used for the treatment of hyperlipidemia. Due to its widespread use and incomplete removal, this compound has been frequently detected in municipal sewage,[3] groundwater,[4] rivers,[5] water reservoirs and tap water.[6] There is evidence that BZF is a potential endocrine disruptor in male zebrafish,[7] and its biomagnification could occur *via* the food chain.[8]

Because fibrate compounds are refractory to biological degradation, traditional wastewater treatment technologies cannot effectively remove BZF.[3] Using chemical techniques to oxidize BZF may have good removal efficiencies, especially for advanced oxidation processes (AOPs) treatment.[9,10] AOPs involve the production of strongly oxidizing hydroxyl radicals ($HO^{\bullet}$) and have been recommended as efficient technologies for water treatment.[11,12] However, chemical reagents storage and formation of potentially toxic byproducts may limit their practical application.[13] Adsorption is an alternative PPCPs removal technology that has a high efficiency and nearly no byproduct generation.[14] This method has been wildly applied in wastewater and drinking water purification.[15] Selection of effective and recyclable adsorbent is critical for the adsorptive treatment.

In the last decade, many adsorbents have been investigated for PPCPs removal from aqueous solution, including porous carbon materials,[16] metal–organic frameworks (MOFs),[17] zeolite,[18] molecular sieve,[19] *etc.* However, the application of the adsorbents is usually limited by high cost, difficulty in separation and regeneration. Recently, researchers are focused on the adsorbents that have high efficiency, safety and regeneration capacity.[14] Carbon nanomaterials, such as graphene-based nanomaterials and carbon nanotubes (CNTs), have been found to be efficient and economic adsorbents for the adsorptive removal of aqueous antibiotics.[16] Carboxyl modification could enhance CNTs adsorptive removal of the pharmaceutical drug from aqueous solution.[20] Nevertheless, poor separability also restricts their practical application, and the release of CNTs during water treatment could induce secondly pollution.[21,22] Using magnetic nanomaterials modified CNTs maybe a possible way to overcome this defect. Among the various magnetic materials, ferrites exhibit high efficiency and are environmentally friendly.[23,24] Some ferrites, such as $MnFe_2O_4$

[a]*Key Laboratory of Integrated Regulation and Resource Development on Shallow Lakes of Ministry of Education, College of Environment, Hohai University, Nanjing 210098, China. E-mail: ghlu@hhu.edu.cn*

[b]*College of Hydraulic and Civil Engineering, XiZang Agricultural and Animal Husbandry College, Linzhi, 860000, China*

[c]*Henan Province Hydrology and Water Resources Bureau, Zhengzhou, 450004, China*

† Electronic supplementary information (ESI) available. See DOI: 10.1039/c7ra07260k

This journal is © The Royal Society of Chemistry 2017

Open Access Article. Published on 14 August 2017. Downloaded on 2/18/2026 4:08:23 AM.
This article is licensed under a Creative Commons Attribution-NonCommercial 3.0 Unported Licence.

and $CoFe_2O_4$, are excellent adsorbents, and their magnetic properties ensure that they can be magnetically separated.[25] Furthermore, synergistic adsorptive removal of heavy metals from aqueous solution has been reported for combined application of ferrite and carbon materials.[26] Considering the excellent performance and low cost, ferrites may be applicable to modify CNTs for adsorptive water treatment. However, the effects of ferrite on the performance of CNTs are largely unknown, and few systematic studies have examined the use of ferrite/CNTs for the adsorptive treatment of BZF containing wastewater.

This work mainly focused on four aspects: (I) preparation and characterization of ferrite modified CNTs adsorbents (MFe_2O_4/CNTs, M: Mn or Co); (II) efficiency of BZF removal by MFe_2O_4/CNTs adsorption; (III) examination of adsorption kinetics, isotherms, and thermodynamics; (IV) investigation of the possible adsorption mechanism.

2. Materials and methods

2.1. Materials and reagents

Multi-walled CNTs (purity > 98%, 30–50 nm of outer diameter) were bought from Chengdu Organic Chemistry Co., Ltd, Chinese Academy of Sciences; BZF was purchased from Sigma Aldrich, and its physicochemical properties and structure are provided in Table S1.† Methanol with HPLC grade was supplied by Merck & Co. The other chemicals (*e.g.*, $Fe(NO_3)_3 \cdot 9H_2O$, $CoCl_2 \cdot 6H_2O$, $MnCl_2 \cdot 4H_2O$, HNO_3, and polyethylene glycol) were analytical grade without any further purification. Ultrapure water (18.25 MΩ cm, Milli-Q, Millipore, Billerica, MA, USA) was used throughout the experimental process.

2.2. Synthesis of MFe_2O_4/CNTs

CNTs were pretreated by 65 wt% HNO_3 solution to remove surface impurities and reduce agglomeration according to the procedure described elsewhere,[27] except that the reaction was carried out in a Teflon-lined stainless-steel autoclave.

Since $MnFe_2O_4$ and $CoFe_2O_4$ have been proven to have good adsorbing properties for water purification,[28] they were employed to modify CNTs, respectively. The MFe_2O_4/CNTs (M: Mn or Co) were synthesized using a hydrothermal method under magnetic stirring. Briefly, 5.0 mmol $Fe(NO_3)_3$ and 2.5 mmol $MnCl_2$, or $CoCl_2$ were added to 10 mL of ultrapure water under magnetic stirring. After the mixture was completely dissolved, 20 mL of polyethylene glycol was added to the solution and stirring continued for 30 min. Then approximately 0.6 g of the acid-treated CNTs were impregnated into the solution with continuous magnetic stirring for 30 min. After that, 2 mol L^{-1} NaOH solution was added dropwise to the mixture with stirring at 400 rpm for 30 min until the pH value reached 11. Thereafter, the suspension was transferred to a 100 mL Teflon-lined stainless-steel autoclave, sealed and hydrothermally treated at 180 °C for 24 h. After cooling to room temperature, the material was collected by a magnet and washed repeatedly with ethanol and ultrapure water. It was finally dried in an oven at 60 °C for 12 h. The products were denoted as MFe_2O_4/CNTs (M: Mn or Co). MFe_2O_4 were prepared by the same method, except the absence of CNTs.

2.3. Experimental set-up and conditions

A stock solution (1.0 g L^{-1}) of the BZF was first prepared in phosphate buffer solution (pH 7.2) and stored in the dark at 4 °C. Experimental solution was prepared by diluting the stock solution in ultrapure water.

In a typical adsorption test, 0.02 g of the adsorbent was mixed with 100 mL of the BZF solution under stirring at 25 °C. After a specified time, the sample was harvested, and filtered through a 0.22 μm membrane to separate the adsorbents and solution. Then the residual BZF concentration in the separated solution was determined. The amount of adsorbed BZF is given by the following equation.

$$q_e = \frac{(C_0 - C_e) \times V}{m} \quad (1)$$

where q_e is the equilibrium adsorption capacity, mg g^{-1}; C_0 is the initial concentration of BZF, mg L^{-1}; C_e is the final or equilibrium BZF concentration, mg L^{-1}; V is the volume of solution, L; m is the mass of adsorbent, g.

To evaluate the reusability of the adsorbents, 0.02 g of MFe_2O_4/CNTs were first put in contact with 100 mL of 20 mg L^{-1} BZF for 24 h. After adsorption, the adsorbents were separated by a magnet, and then dried at 40 °C for 24 h. Desorption processes were conducted by mixing 0.01 g of the above mentioned dried adsorbents with 60 mL of methanol for 30 min. Finally, the concentration of BZF in the methanol after desorption was measured. The desorption efficiency was calculated as:

$$\text{Desorption ratio (\%)} = \frac{\text{amount of desorbed BZF}}{\text{amount of adsorbed BZF}} \times 100 \quad (2)$$

2.4. Analytical methods

The X-ray diffraction (XRD, Dmax-RB, Rigaku Corporation, Tokyo, Japan) equipped with a copper anode generating Cu Kα radiation was used to investigate the crystal structure of MFe_2O_4/CNTs samples with a scanning range of 20–80°, scanning step of 0.02°, and stepping rate of 8° min^{-1}. The morphologies were characterized by using a transmission electron microscope (TEM, JEM-200CX, JEOL Corporation, Tokyo, Japan) operated at 200 kV. Fourier Transform Infrared Spectroscopy (FT-IR) was recorded on FT-IR Nicolet iS10 (Thermo Fisher Scientific, USA) from 400 to 4000 cm^{-1}. The constituents of MFe_2O_4/CNTs and the chemical analysis of the surface elements were determined by X-ray photoelectron spectroscopy (XPS, PHI 5000, ULVAC-PHI, Japan). Measurements of Brunauer–Emmett–Teller (BET) surface area and pore size distribution were performed using N_2 adsorption/desorption isotherms on a BelSorp-Mini (Bayer Corporation, Tokyo, Japan). The thermal stability and purity were analyzed by thermogravimetric-differential scanning calorimetry (TG-DSC, STA 409 PC/PG, Germany). Vibrating sample magnetometer (VSM, Lakeshore 7407, USA) was used to measure the magnetic

Open Access Article. Published on 14 August 2017. Downloaded on 2/18/2026 4:08:23 AM.
This article is licensed under a Creative Commons Attribution-NonCommercial 3.0 Unported Licence.

prosperities of the materials. The point of zero charge measurements and Boehm titration were performed according to the procedures described in elsewhere.[29] High-performance liquid chromatographic (HPLC, Waters Alliance e2998, USA) method was established for the determination of BZF, and samples were performed on SunFire C18 of phosphate buffer (0.01 mol L^{-1} at pH 3.5)–methanol–acetonitrile (40 : 15 : 45, v/v/v) as mobile phase, at a flow rate of 1 mL min^{-1}. The pH value and temperature were determined by a Thermo Orion 868 meter (USA).

3. Results and discussion

3.1. Characterization of MFe_2O_4/CNTs

Fig. 1 shows the XRD patterns of acid-treated CNTs, MFe_2O_4 and MFe_2O_4/CNTs. There were seven characteristic diffraction peaks in $MnFe_2O_4$/CNTs at $2\theta = 29.71°$, 34.98°, 36.65°, 42.53°, 52.74°, 56.20° and 61.66°, which corresponded to the (220), (311), (222), (400), (422), (511) and (440) facets of the face-centered cubic spinel structures of $MnFe_2O_4$ (JCPDS no. 10-0319).[30] $CoFe_2O_4$/CNTs were compared with standard spectra JCPDS no. 22-1086,[26] implying that 2θ values of 30.08°, 35.44°, 37.06°, 43.06°, 53.45°, 56.97° and 62.59° corresponded to (220), (311), (222), (400), (422), (511) and (440) facets of face-centered cubic spinel structure. The additional peak at around 26.06° was assigned to (002) lattice plane of the CNTs.[31] There was no obvious difference in ferrite diffraction peaks between MFe_2O_4 and MFe_2O_4/CNTs.

The morphology and microstructure of the prepared MFe_2O_4/CNTs was investigated by TEM (Fig. 2). Compared to unmodified CNTs (Fig. S1 in ESI†), the MFe_2O_4 nanoparticles were randomly attached on the CNTs, and sizes of MFe_2O_4 were from 10 to 30 nm. Fig. 3 displays the FT-IR spectra of the acid-treated CNTs and MFe_2O_4/CNTs. The characteristic absorbance peak at 3442 cm^{-1} represents –OH group and at 1631 cm^{-1} corresponds to –COOH group.[32] For MFe_2O_4/CNTs samples, the peak at 550–600 cm^{-1} was related to the metal–oxygen stretching mode from the ferrites.[33] In addition, existing 2847–2945 cm^{-1} (C–H stretching) peaks and bands at 1274 cm^{-1} and 715 cm^{-1} were related to stretching of C–O bonds and metal–oxygen deformation, respectively.[34] The surface chemistry of

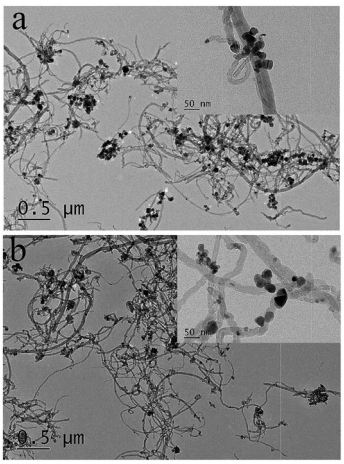

Fig. 2 TEM micrographs of $MnFe_2O_4$/CNTs (a) and $CoFe_2O_4$/CNTs (b).

MFe_2O_4/CNTs obtained by Boehm titration are summarized in Table S2,† which was consistent with FT-IR characterization. Relationship of ΔpH (*i.e.* $pH_{final} - pH_{initial}$) and $pH_{initial}$ was obtained in Fig. S2,†[29] and the point of intersection gave the pH_{PZC} of the $MnFe_2O_4$/CNTs and $CoFe_2O_4$/CNTs were ~3.5 and ~4.0, respectively.

To characterize the surface components and the elements valences of the composites, the materials were subjected to XPS analysis. The C 1s, O 1s, Mn 2p, Co 2p and Fe 2p core photo-ionization signals were shown in the XPS full spectrum scans (Fig. S3† and 4). The C 1s characteristic peaks appearing at 284.5 eV and 285.1 eV are assigned to C–C and C=C bonds for CNTs, respectively.[26,35] The O 1s consist of three peaks that are assigned to Fe–O (529.9 eV for $MnFe_2O_4$/CNTs and 529.8 eV for $CoFe_2O_4$/CNTs), C=O (531.0 eV for $MnFe_2O_4$/CNTs and 531.6 eV for $CoFe_2O_4$/CNTs) and C–O (533.0 eV for $MnFe_2O_4$/CNTs and 533.1 eV for $CoFe_2O_4$/CNTs) bonds,[36] indicating the introduction of new functional groups on the surfaces of MFe_2O_4/CNTs and consistency with the FT-IR analysis results. The Co 2p spectrum indicates Co existence in the Co^{2+} species, because the Co^{3+} cations can only be paired in weaker electron orbits.[37] The peaks of Mn $2p_{3/2}$ and Mn $2p_{1/2}$ individually appeared at 641.0 and 652.2 eV referring to Mn(II), and Fe 2p at around 710.0 eV signified the existence of Fe^{3+}.[38,39]

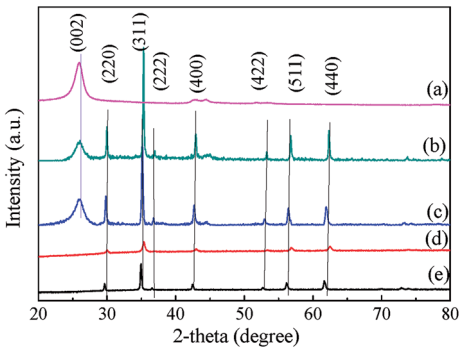

Fig. 1 XRD patterns of CNTs (a), $CoFe_2O_4$/CNTs (b), $MnFe_2O_4$/CNTs (c), $CoFe_2O_4$ (d) and $MnFe_2O_4$ (e).

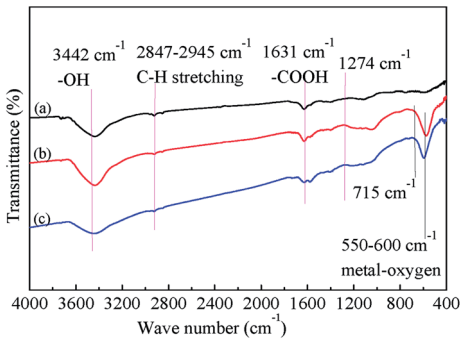

Fig. 3 FT-IR spectra of CNTs (a), $MnFe_2O_4$/CNTs (b) and $CoFe_2O_4$/CNTs (c).

Open Access Article. Published on 14 August 2017. Downloaded on 2/18/2026 4:08:23 AM.
This article is licensed under a Creative Commons Attribution-NonCommercial 3.0 Unported Licence.

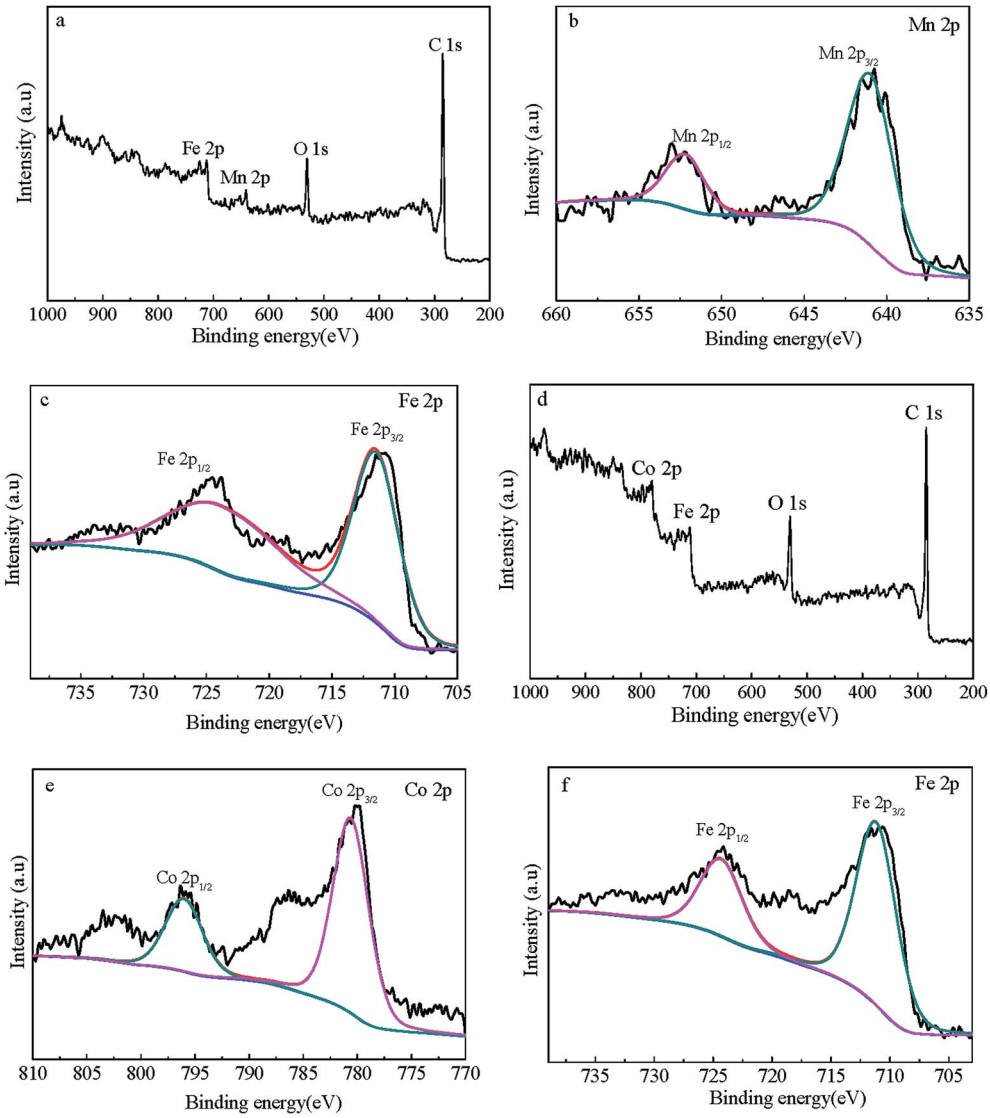

Fig. 4 XPS wide-scan (a), Mn 2p spectra (b) and Fe 2p spectra (c) of $MnFe_2O_4$/CNTs; XPS wide-scan (d), Co 2p spectra (e) and Fe 2p spectra (f) of $CoFe_2O_4$/CNTs.

Nitrogen adsorption–desorption isotherms of the adsorbents were H1-type hysteresis loops and the pore size was mainly mesopore distribution (Fig. 5), this indicates that the samples were mesoporous materials.[40] Specific surface area, total pore volume and average pore size of the acid-treated CNTs and MFe_2O_4/CNTs are summarized in Table 1. Compared to CNTs, these parameters were decreased for the MFe_2O_4/CNTs. This phenomenon is in accordance with results in previous reports, which indicated that ferrite particles have much smaller surface area and pore volume as compared to CNTs.[26] TG curves (Fig. 6) clearly show that the mass fractions were finally maintained at 52.5% for $MnFe_2O_4$/CNTs and 47.5% for $CoFe_2O_4$/CNTs, respectively. Peaks at 480–510 °C on DSC traces indicate that MFe_2O_4/CNTs were thermally stable until the temperature reached over 480 °C. The saturation magnetization of $MnFe_2O_4$/CNTs and $CoFe_2O_4$/CNTs were 23.8 and 26.1 emu g^{-1}, respectively (Fig. 7). It was reported that the composite with a saturation magnetization over 16.3 emu g^{-1} had a strong magnetic response capability.[38] Therefore, the prepared $MnFe_2O_4$/CNTs could be magnetically separated from wastewater, which was verified by a direct magnetic experiment (photo in Fig. 7).

3.2. Adsorption and desorption performances

As shown in Fig. 8, the adsorption tendencies were similar for various adsorbents. The BZF was rapidly adsorbed within the initial 2 min, and then it continued at a relatively smaller adsorption rate and finally achieved equilibrium at around 20 min. This observation is consistent with the results in literatures.[23,40] For adsorbents with a large amount of surface active sites, initial surface diffusion between the solid phase and the liquid phase was fast.[41] The following slower adsorption rate was related to intraparticle diffusion that affected the overall adsorption time. $MnFe_2O_4$ and $CoFe_2O_4$ were inefficient for adsorptive

Open Access Article. Published on 14 August 2017. Downloaded on 2/18/2026 4:08:23 AM.
This article is licensed under a Creative Commons Attribution-NonCommercial 3.0 Unported Licence.

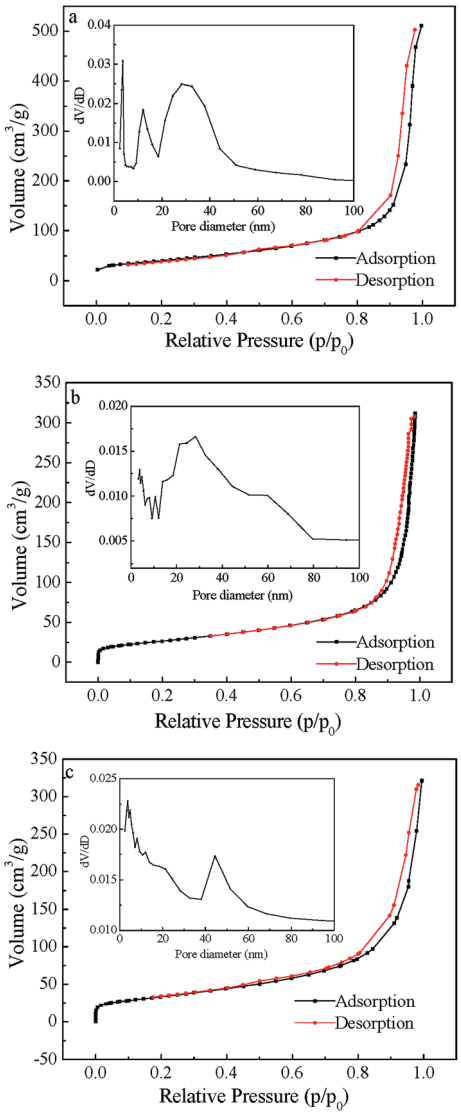

Fig. 5 Nitrogen adsorption–desorption isotherms of CNTs (a), $MnFe_2O_4$/CNTs (b) and $CoFe_2O_4$/CNTs (c). (The inset shows the pore size distribution curves).

Table 1 The physical properties of CNTs and MFe_2O_4/CNTs

Material	S_{BET} (m^2 g^{-1})	V_{total} (cm^3 g^{-1})	Average pore size (nm)
CNTs	145.92	0.7618	20.883
$MnFe_2O_4$/CNTs	96.526	0.4827	20.003
$CoFe_2O_4$/CNTs	120.67	0.4647	15.405

removal of BZF. Although the adsorption capacity of CNTs decreased after ferrite modification, the MFe_2O_4/CNTs also showed to be effective for BZF removal, the maximum adsorption capacities of $MnFe_2O_4$/CNTs and $CoFe_2O_4$/CNTs for BZF were 30.1 and 24.5 mg g^{-1}, respectively. Compared to $CoFe_2O_4$/CNTs, $MnFe_2O_4$/CNTs had a smaller specific surface area but exhibited a higher BZF adsorption capacity, implying that the surface

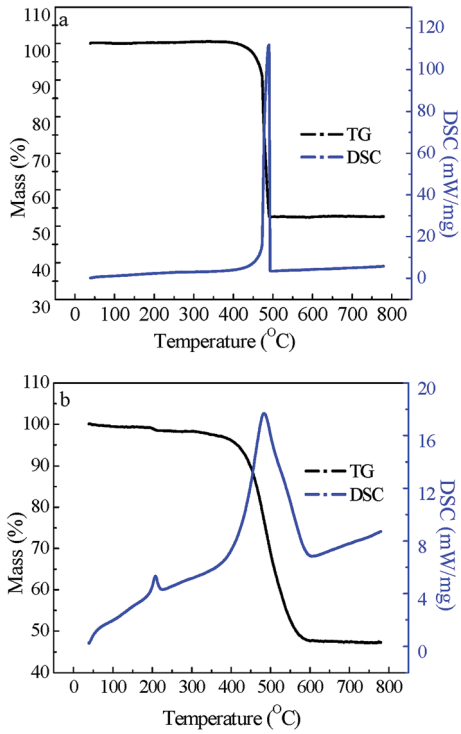

Fig. 6 TG-DSC curves of $MnFe_2O_4$/CNTs (a) and $CoFe_2O_4$/CNTs (b).

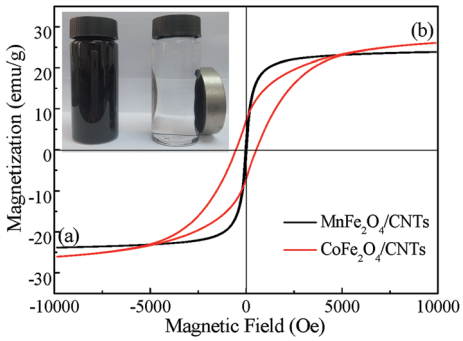

Fig. 7 *M–H* hysteresis loops of $MnFe_2O_4$/CNTs (a) and $CoFe_2O_4$/CNTs (b). (The inset shows the magnetic characterization of MFe_2O_4/CNTs *via* an external magnetic field).

functional groups, the active surface sites and particle size might also be influence factors for adsorption capacities. A similar inference was suggested by previous reports.[28,42]

Fig. 9 shows the effects of initial BZF concentration on the adsorption efficiency of the MFe_2O_4/CNTs. When the initial BZF concentration varied from 5 to 40 mg L^{-1}, the maximum adsorption capacities of $MnFe_2O_4$/CNTs and $CoFe_2O_4$/CNTs for BZF increased from 14.8 to 33.4 mg g^{-1} and 8.1 to 27.8 mg g^{-1}, respectively. The initial concentration of BZF had a great influence on the saturated adsorption capacity of MFe_2O_4/CNTs.

Besides the adsorption performance, the recycling and reuse ability of the adsorbent are also important for its application. Methanol was used as the desorption agent due to its weak polarity.[43] The calculated desorption efficiencies of the

Open Access Article. Published on 14 August 2017. Downloaded on 2/18/2026 4:08:23 AM.
This article is licensed under a Creative Commons Attribution-NonCommercial 3.0 Unported Licence.

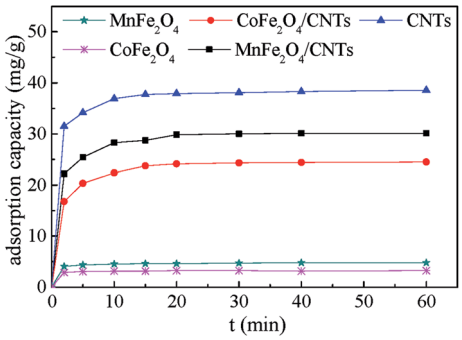

Fig. 8 Adsorption capacity of various adsorbents. (Initial BZF concentration 20 mg L^{-1}, adsorbent dosage 0.02 g, neutral pH and temperature 25 °C).

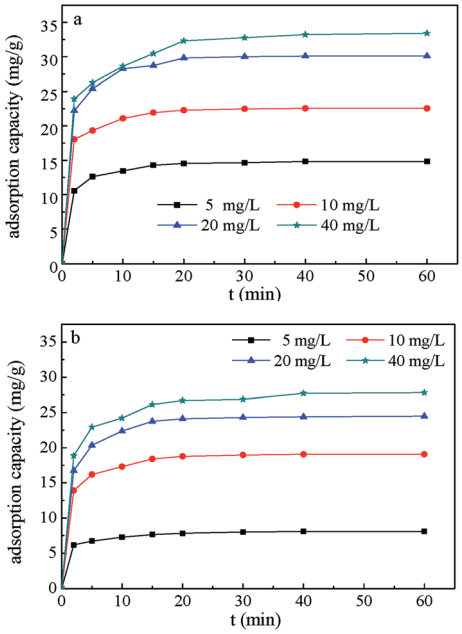

Fig. 9 Effects of initial BZF concentration on the adsorption efficiency of $MnFe_2O_4$/CNTs (a) and $CoFe_2O_4$/CNTs (b). (Adsorbent dosage 0.02 g, neutral pH and temperature 25 °C).

$MnFe_2O_4$/CNTs and $CoFe_2O_4$/CNTs were 82.4% and 76.0%, respectively, confirming a good desorption performance of MFe_2O_4/CNTs.

3.3. Adsorption isotherms

The Langmuir and Freundlich isotherms, two commonly used adsorption isotherm models,[44,45] were fitted to explore the interaction between the adsorbents and contaminant (eqn (3) and (4)).

$$\frac{1}{q_e} = \frac{1}{q_{max}} + \frac{1}{K_L q_{max}} \frac{1}{C_e} \quad (3)$$

$$\log q_e = \log K_F + \frac{1}{n} \log C_e \quad (4)$$

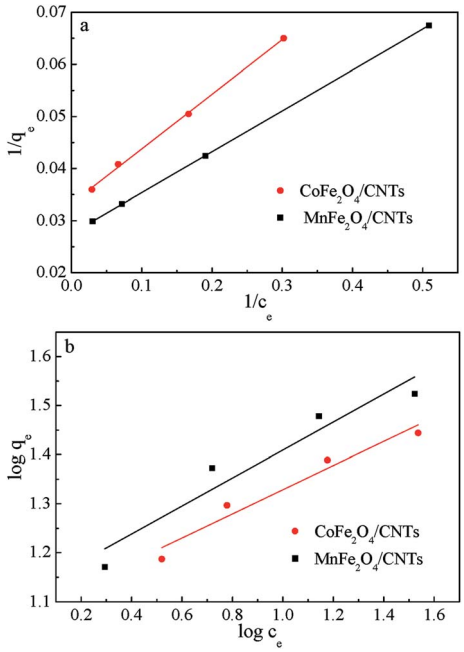

Fig. 10 Adsorption isotherm models of BZF: Freundlich (a) and Langmuir (b). (Adsorbent dosage 0.02 g, neutral pH and temperature 25 °C).

where q_e is the amount of BZF adsorbed per unit mass of the MFe_2O_4/CNTs, mg g^{-1}; q_{max} is the maximum adsorption capacity, mg g^{-1}; C_e is the aqueous equilibrium concentration of BZF, mg L^{-1}; K_L is the Langmuir adsorption affinity parameter, L mg^{-1}. K_F and $1/n$ are the Freundlich isotherm constants.

Fig. 10 shows the Langmuir and Freundlich isotherms based on the experimental data, and the parameters calculated from linear regression are listed in Table 2. The maximum adsorption capacities toward BZF calculated by Langmuir equation were 35.5 mg g^{-1} for $MnFe_2O_4$/CNTs and 29.1 mg g^{-1} for $CoFe_2O_4$/CNTs, and the correlation coefficients (R^2) of the Langmuir model are over 0.99. These results suggest that MFe_2O_4/CNTs have great potential for BZF removal and the Langmuir isotherm fits the experimental data better than Freundlich isotherm. The Langmuir isotherm implies that a monolayer-type adsorption of BZF onto the sorption sites of MFe_2O_4/CNTs.[40]

The Dubinin–Radushkevich isotherm was applied to express the adsorption mechanism and distinguish the physical and chemical adsorption of BZF on MFe_2O_4/CNTs with its mean free energy.[46,47] The calculated sorption means free energy for the $MnFe_2O_4$/CNTs and $CoFe_2O_4$/CNTs from the Dubinin–Radushkevich isotherm were 4.6 and 4.5 kJ mol^{-1}, respectively (Table S3†), indicating multiple adsorption interactions such as van der Waals, hydrogen and π–π bonding may mainly affect the adsorption mechanism.[48]

3.4. Adsorption kinetics

3.4.1 Pseudo-first-order and pseudo-second-order models. The pseudo-first-order (eqn (5)) and pseudo-second-order (eqn (6)) kinetic models were suitably applied to analyze the process of magnetic ferrite adsorption.[37]

Open Access Article. Published on 14 August 2017. Downloaded on 2/18/2026 4:08:23 AM.
This article is licensed under a Creative Commons Attribution-NonCommercial 3.0 Unported Licence.

Table 2 Parameters of Freundlich and Langmuir adsorption isotherm models for BZF adsorption on MFe_2O_4/CNTs. (Adsorbent dosage 0.02 g, neutral pH and temperature 25 °C)

	Langmuir model			Freundlich model		
Adsorbent	q_{max} (mg g^{-1})	K_L (L mg^{-1})	R_L^2	K_F	n	R_F^2
$MnFe_2O_4$/CNTs	35.5	0.3606	0.9999	3.04	3.43	0.9298
$CoFe_2O_4$/CNTs	29.1	0.3340	0.9983	2.91	3.94	0.9574

Table 3 Adsorption parameters got from kinetic for the adsorption of BZF on MFe_2O_4/CNTs. (Initial BZF concentration 20 mg L^{-1}, adsorbent dosage 0.02 g, neutral pH and temperature 25 °C)

	Pseudo-first-order			Pseudo-second-order		
Adsorbent	K_1 (1/min)	q_e (mg g^{-1})	R_1^2	K_2 (g (mg min)$^{-1}$)	q_e (mg g^{-1})	R_2^2
$MnFe_2O_4$/CNTs	0.5359	27.18	0.9382	0.0407	30.67	0.9999
$CoFe_2O_4$/CNTs	0.2701	6.60	0.9737	0.0427	25.00	0.9999

$$\log(q_e - q_t) = \log q_e - \frac{K_1 t}{2.303} \quad (5)$$

$$\frac{t}{q_t} = \frac{1}{K_2 q_e^2} + \frac{t}{q_e} \quad (6)$$

where q_e and q_t are the amount of BZF adsorbed at equilibrium and at time (t), respectively, mg g^{-1}; K_1 (1/min) and K_2 (g (mg min)$^{-1}$) are the pseudo-first-and second-order rate constant, respectively.

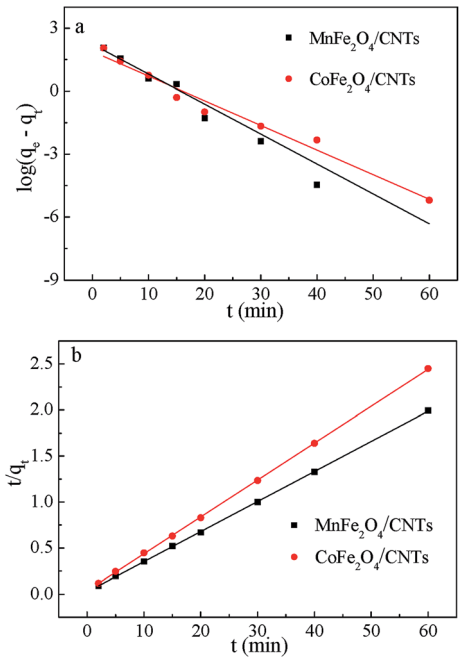

Fig. 11 Kinetic curves of BZF adsorption on MFe_2O_4/CNTs: Pseudo-first-order model (a) and Pseudo-second-order model (b). (Initial BZF concentration 20 mg L^{-1}, adsorbent dosage 0.02 g, neutral pH and temperature 25 °C).

The calculated data (Table 3 and Fig. 11) reveal that the higher correlation coefficients (R^2) of the pseudo-second-order model was over 0.99, and the calculated q_e values were consistent better with experimental values, as compared to the pseudo-first-order model. A better agreement with pseudo-second-order model indicates that the adsorption mechanism depended on the MFe_2O_4/CNTs and BZF molecule.[23,49]

3.4.2 Weber and Morris model. The Weber and Morris model could be used to assess and differentiate the effect of the boundary layer and intraparticle diffusion on adsorption progress.[50] It can be described as eqn (7).

$$q_t = K_{WM}\sqrt{t} + L \quad (7)$$

where q_t is the amount of BZF adsorbed on the adsorbent at the time (t), mg g^{-1}; K_{WM} is the internal diffusion coefficient; t is the adsorption time, min; L is the thickness of the boundary layer.

The results in Fig. 12 show that the straight lines did not pass through the origin and values of R^2 were less than 0.66, indicating that the internal diffusion model could not fully fit the adsorption process, and internal diffusion was not the only factor controlling the adsorption process.[51] The boundary layer effect of $MnFe_2O_4$/CNTs was greater than that of $CoFe_2O_4$/CNTs according to the intercept value. In general, as the boundary layer increased, the surface flux increased too, allowing a faster adsorption of BZF molecules towards the inside of the MFe_2O_4/CNTs pores. This phenomenon is consistent with the actual adsorption process from the straight slopes in Fig. 8 and 9.

3.4.3 Boyd model. The adsorption process was found to be controlled by external mass transfer and intra-particle diffusion, thus, the actual rate-controlling step was further analyzed by Boyd model.[52] The kinetic model expression can be written as follows.[53]

$$Bt = -0.4977 - \ln\left(1 - \frac{q_t}{q_e}\right) \quad (8)$$

Open Access Article. Published on 14 August 2017. Downloaded on 2/18/2026 4:08:23 AM.
This article is licensed under a Creative Commons Attribution-NonCommercial 3.0 Unported Licence.

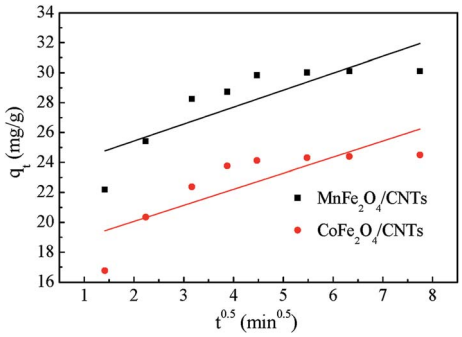

Fig. 12 Weber and Morris kinetic model of BZF adsorption on MFe_2O_4/CNTs. (Initial BZF concentration 20 mg L^{-1}, adsorbent dosage 0.02 g, neutral pH and temperature 25 °C).

$$B = \frac{\pi^2 D_i}{r^2} \tag{9}$$

where q_e and q_t are the amount of BZF adsorbed at equilibrium and at time (t), respectively, mg g^{-1}; D_i (cm^2 s^{-1}) are the effective diffusion coefficient and r represents the radius of adsorbent particles assumed to be spherical.

The linearity test of Bt *vs.* t plots were employed to find out the particle diffusion control mechanism. Fig. 13 shows the plots of MFe_2O_4/CNTs were linear and did not pass through the origin, indicating that external mass transfer mainly affected the rate-controlling process and intraparticle diffusion showed a relatively weak rate control for BZF adsorption onto MFe_2O_4/CNTs. These results were in good agreement with the analysis of Weber and Morris model and a similar control mechanism had been reported by Kumar *et al.*[54]

3.5. Adsorption thermodynamics

The feasibility of the adsorption process was also evaluated by thermodynamics analysis. Gibbs free energy (ΔG^o) using the following equation (eqn (10)) and K_d was the distribution constant calculated by eqn (11).[55]

$$\Delta G^o = -RT \ln K_d \tag{10}$$

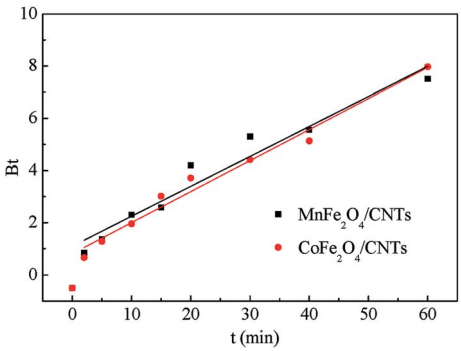

Fig. 13 Boyd model of BZF adsorption on MFe_2O_4/CNTs. (Initial BZF concentration 20 mg L^{-1}, adsorbent dosage 0.02 g, neutral pH and temperature 25 °C).

$$K_d = \frac{q_e}{C_e} \tag{11}$$

where R is the universal gas constant (8.314×10^{-3} kJ (mol K)$^{-1}$); T is 298 K; q_e is the amount of BZF adsorbed on the MFe_2O_4/CNTs, mg g^{-1}; C_e is equilibrium concentration of BZF in the solution, mg L^{-1}.

With the initial BZF concentration of 20 mg L^{-1}, ΔG^o of BZF adsorbed on the MFe_2O_4/CNTs were negative values, suggesting that the adsorption processes were spontaneous. The greater the ΔG^o, the smaller the spontaneous trend.[56] The calculated ΔG^o for the $MnFe_2O_4$/CNTs and $CoFe_2O_4$/CNTs were −1.9 and −1.2 kJ mol^{-1}, displaying that the adsorption process of the $MnFe_2O_4$/CNTs was more spontaneous than the $CoFe_2O_4$/CNTs.

3.6. Adsorption mechanism

Generally, the adsorption mechanisms of the aqueous organic pollutants on ferrites and carbon-based porous adsorbents involve the surface diffusion, pore diffusion and adsorption reactions.[50,57] Although the mechanism of BZF adsorbed on the MFe_2O_4/CNTs is not yet clear, several points could be raised in order to discuss the adsorption process. It is reported that the specific surface area, surface functional group and boundary layer jointly affect the performance of the adsorption site, thereby affecting the surface diffusion.[41] The BET and FT-IR analyses (Table 1 and Fig. 3) indicate that ferrite modification changed the specific surface area and surface functional groups of the CNTs. However, the comparison tests (Fig. 8) imply that the introduced ferrite did not dominate the BZF adsorption on the MFe_2O_4/CNTs, and the process might be mainly determined by the CNTs. The Langmuir model suggests the applicability of monolayer coverage of BZF molecules on the surface of MFe_2O_4/CNTs. Surface diffusion governs the surface flux of BZF, having a significant effect on the overall intraparticle diffusion. On the other hand, based on the results of the pore size distribution (Fig. 5) and the Weber and Morris model (Fig. 12), it can be speculated that the pore diffusion is mainly controlled by the porosity, adsorption sites within the pores, and blocking effect. The adsorption reactions occur at the adsorption site, through the entire adsorption process, being a dynamic balancing process. In summary, the amount of adsorbent surface and internal adsorption site determines the amount of adsorption, while the porosity and the properties of the surface layer

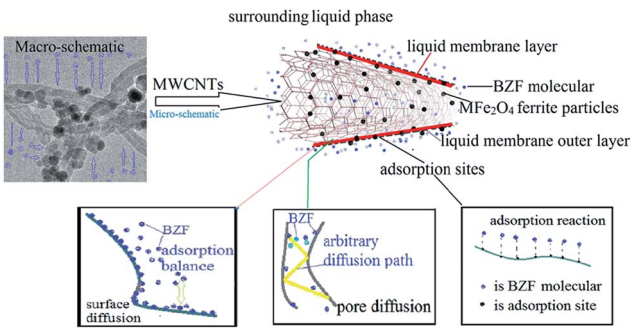

Fig. 14 Possible mechanism of BZF adsorption on MFe_2O_4/CNTs.

Open Access Article. Published on 14 August 2017. Downloaded on 2/18/2026 4:08:23 AM.
This article is licensed under a Creative Commons Attribution-NonCommercial 3.0 Unported Licence.

determine the adsorption rate. The possible adsorption mechanism is shown in Fig. 14.

It should be noted that the results of this study were obtained with synthetic BZF solutions. The determined pH_{PZC} values for MFe_2O_4/CNTs were lower than the pH of the current reaction solution (~7.0). This fact suggests negative charge exists on the surface of MFe_2O_4/CNTs, promoting cationic adsorption during the adsorption process.[24,58] In addition, $\log K_{ow}$ and $\log K_{oc}$ of BZF are 4.25 and 1.0 at pH = 7.4,[59] respectively, indicating that BZF has a high tendency to sorb onto the organic material. For practical application, the water matrix such as pH and organic carbon content, may have significant effects on BZF adsorption. Due to the complex compositions of real water or wastewaters, more studies are required to further elucidate the adsorption behavior and mechanism.

4. Conclusions

The mesoporous MFe_2O_4/CNTs with large surface area and good dispersity were synthesized for the adsorptive removal of BZF. Characterization results in conjunction with experimental data demonstrated the high efficiency and recyclability of the fabricated MFe_2O_4/CNTs. Restated, not only BZF containing wastewater could be purified, but also the used adsorbents could be easily magnetically separated and regenerated. The spontaneous adsorption processes could be well described by Langmuir isotherm model and pseudo-second-order equation. The porosity and adsorption sites within pores had a synergistic effect on the rate of pore diffusion, and the amount of adsorption site would substantially affect the saturated adsorption.

Conflicts of interest

The authors declare no competing financial interest.

Acknowledgements

We are grateful for grants from the National Natural Science Foundation of China (No. 51608167), Scientific and Technological Project of Henan Province (No. 162102310057), and A Project Funded by the Priority Academic Program Development of Jiangsu Higher Education Institutions.

References

1 J. Wang and S. Wang, *J. Environ. Manage.*, 2016, **182**, 620–640.
2 J.-L. Liu and M.-H. Wong, *Environ. Int.*, 2013, **59**, 208–224.
3 C. I. Kosma, D. A. Lambropoulou and T. A. Albanis, *Sci. Total Environ.*, 2014, **466**, 421–438.
4 Z. Li, X. Xiang, M. Li, Y. Ma, J. Wang and X. Liu, *Ecotoxicol. Environ. Saf.*, 2015, **119**, 74–80.
5 F. O. Agunbiade and B. Moodley, *Environ. Toxicol. Chem.*, 2016, **35**, 36–46.
6 I. Zaibel, D. Zilberg, L. Groisman and S. Arnon, *Sci. Total Environ.*, 2016, **559**, 268–281.
7 Y. M. Velasco-Santamaría, B. Korsgaard, S. S. Madsen and P. Bjerregaard, *Aquat. Toxicol.*, 2011, **105**, 107–118.
8 T. Malchi, Y. Maor, G. Tadmor, M. Shenker and B. Chefetz, *Environ. Sci. Technol.*, 2014, **48**, 9325–9333.
9 H. Yuan, Y. Zhang and X. Zhou, *Clean: Soil, Air, Water*, 2012, **40**, 239–245.
10 M. M. Huber, S. Canonica, G.-Y. Park and U. Von Gunten, *Environ. Sci. Technol.*, 2003, **37**, 1016–1024.
11 D. Wu, R. Zhang, G. Lu, Q. Lin, F. Liu and Y. Li, *Clean: Soil, Air, Water*, 2017, **45**, 1500664.
12 D. Wu, G. Lu, R. Zhang, H. You, Z. Yan and Y. Li, *Water Sci. Technol.: Water Supply*, 2016, **16**, 163–170.
13 C. Gadipelly, A. Pérez-González, G. D. Yadav, I. Ortiz, R. Ibáñez, V. K. Rathod and K. V. Marathe, *Ind. Eng. Chem. Res.*, 2014, **53**, 11571–11592.
14 A. Carmalin Sophia, E. C. Lima, N. Allaudeen and S. Rajan, *Desalin. Water Treat.*, 2016, **57**, 27573–27586.
15 J. He, K. Chen, X. Cai, Y. Li, C. Wang, K. Zhang, Z. Jin, F. Meng, X. Wang and L. Kong, *J. Colloid Interface Sci.*, 2017, **490**, 97–107.
16 F. Yu, Y. Li, S. Han and J. Ma, *Chemosphere*, 2016, **153**, 365–385.
17 N. Zhuo, Y. Lan, W. Yang, Z. Yang, X. Li, X. Zhou, Y. Liu, J. Shen and X. Zhang, *Sep. Purif. Technol.*, 2017, **177**, 272–280.
18 T. M. Salem Attia, X. L. Hu and D. Q. Yin, *Chemosphere*, 2013, **93**, 2076–2085.
19 W. Chen, X. Li, Z. Pan, Y. Bao, S. Ma and L. Li, *Chem. Eng. J.*, 2015, **281**, 397–403.
20 Z. Chen, D. Pierre, H. He, S. Tan, C. Pham-Huy, H. Hong and J. Huang, *Int. J. Pharm.*, 2011, **405**, 153–161.
21 F. Yu, J. Chen, L. Chen, J. Huai, W. Gong, Z. Yuan, J. Wang and J. Ma, *J. Colloid Interface Sci.*, 2012, **378**, 175–183.
22 Z. Yan, G. Lu, H. Sun and B. Ma, *Chemosphere*, 2017, **178**, 165–172.
23 L. Wang, J. Li, Y. Wang, L. Zhao and Q. Jiang, *Chem. Eng. J.*, 2012, **181**, 72–79.
24 O. A. Oyetade, V. O. Nyamori, B. S. Martincigh and S. B. Jonnalagadda, *RSC Adv.*, 2015, **5**, 22724–22739.
25 W. Sun, W. Pan, F. Wang and N. Xu, *Chem. Eng. J.*, 2015, **273**, 353–362.
26 L. Tan, Q. Liu, X. Jing, J. Liu, D. Song, S. Hu, L. Liu and J. Wang, *Chem. Eng. J.*, 2015, **273**, 307–315.
27 D. Wu, G. Lu, R. Zhang, Q. Lin, J. Yao, X. Shen and W. Wang, *Electrochim. Acta*, 2017, **236**, 297–306.
28 X. Bao, Z. Qiang, W. Ling and J.-H. Chang, *Sep. Purif. Technol.*, 2013, **117**, 104–110.
29 O. A. Oyetade, V. O. Nyamori, B. S. Martincigh and S. B. Jonnalagadda, *RSC Adv.*, 2016, **6**, 2731–2745.
30 M. Balaji, R. Jeyaram and P. Matheswaran, *J. Alloys Compd.*, 2017, **696**, 435–442.
31 L. Zhou, L. Ji, P.-C. Ma, Y. Shao, H. Zhang, W. Gao and Y. Li, *J. Hazard. Mater.*, 2014, **265**, 104–114.
32 X. Zhang, M. Feng, R. Qu, H. Liu, L. Wang and Z. Wang, *Chem. Eng. J.*, 2016, **301**, 1–11.
33 D. Berger, D. Georgescu, L. Bajenaru, A. Zanfir, N. Stănică and C. Matei, *J. Alloys Compd.*, 2017, **708**, 278–284.

 This journal is © The Royal Society of Chemistry 2017

Open Access Article. Published on 14 August 2017. Downloaded on 2/18/2026 4:08:23 AM.
This article is licensed under a Creative Commons Attribution-NonCommercial 3.0 Unported Licence.

34 A. Esmaeili and S. Ghobadianpour, *Ind. Crops Prod.*, 2016, **91**, 44–48.
35 C.-C. Chen, C.-F. Chen, C.-M. Chen and F.-T. Chuang, *Electrochem. Commun.*, 2007, **9**, 159–163.
36 J. Ma, Z. Zhu, B. Chen, M. Yang, H. Zhou, C. Li, F. Yu and J. Chen, *J. Mater. Chem. A*, 2013, **1**, 4662–4666.
37 N. Li, M. Zheng, X. Chang, G. Ji, H. Lu, L. Xue, L. Pan and J. Cao, *J. Solid State Chem.*, 2011, **184**, 953–958.
38 C. Tan, N. Gao, D. Fu, J. Deng and L. Deng, *Sep. Purif. Technol.*, 2017, **175**, 47–57.
39 A. S. Albuquerque, M. V. C. Tolentino, J. D. Ardisson, F. C. C. Moura, R. D. Mendonça and W. A. A. Macedo, *Ceram. Int.*, 2012, **38**, 2225–2231.
40 Q. Hu, Y. Liu, X. Gu and Y. Zhao, *Chemosphere*, 2017, **181**, 328–336.
41 R. Ocampo-Perez, C. G. Aguilar-Madera and V. Díaz-Blancas, *Chem. Eng. J.*, 2017, **321**, 510–520.
42 S. Mishra, J. Dwivedi, A. Kumar and N. Sankararamakrishnan, *RSC Adv.*, 2016, **6**, 95865–95878.
43 M. J. Ahmed and M. Ahmaruzzaman, *J. Environ. Manage.*, 2015, **163**, 163–173.
44 H. Freundlich, *Z. Phys. Chem.*, 1907, **57**, 385–470.
45 I. Langmuir, *J. Am. Chem. Soc.*, 1918, **40**, 1361–1403.
46 M. M. Dubinin, *Chem. Rev.*, 1960, **60**, 235–241.
47 J. P. Hobson, *J. Phys. Chem.*, 1969, **73**, 2720–2727.
48 S. Ahmad, N. Khalid and M. Daud, *Sep. Sci. Technol.*, 2002, **37**, 343–362.
49 B. Czech, *RSC Adv.*, 2016, **6**, 110383–110392.
50 Q. Zhu, G. D. Moggridge and C. D'Agostino, *Chem. Eng. J.*, 2016, **306**, 1223–1233.
51 A. Hovsepyan and J.-C. J. Bonzongo, *J. Hazard. Mater.*, 2009, **164**, 73–80.
52 G. Boyd, A. Adamson and L. Myers Jr, *J. Am. Chem. Soc.*, 1947, **69**, 2836–2848.
53 J. Ma, F. Yu, L. Zhou, L. Jin, M. Yang, J. Luan, Y. Tang, H. Fan, Z. Yuan and J. Chen, *ACS Appl. Mater. Interfaces*, 2012, **4**, 5749–5760.
54 K. V. Kumar, V. Ramamurthi and S. Sivanesan, *J. Colloid Interface Sci.*, 2005, **284**, 14–21.
55 M. Wawrzkiewicz, P. Bartczak and T. Jesionowski, *Int. J. Biol. Macromol.*, 2017, **99**, 754–764.
56 V. S. Munagapati and D. S. Kim, *Ecotoxicol. Environ. Saf.*, 2017, **141**, 226–234.
57 F. Yu, J. Ma, J. Wang, M. Zhang and J. Zheng, *Chemosphere*, 2016, **146**, 162–172.
58 M. A. M. Salleh, D. K. Mahmoud, A. W. A. K. Wan and A. Idris, *Desalination*, 2011, **280**, 1–13.
59 M. Mohd Amin, S. Heijman and L. Rietveld, *Environ. Technol. Rev.*, 2014, **3**, 61–70.